RSC Advances

PAPER

View Article Online
View Journal | View Issue

Cite this: *RSC Adv.*, 2025, **15**, 29822

Improved photocatalytic efficiency of $Sr_5Ta_4O_{15}$ perovskite oxide *via* V doping and oxygen defects

A. Brach, [a] H. Zaari,[a] A. Benyoussef[b] and L. Bahmad *[a]

Received 17th June 2025
Accepted 17th August 2025

DOI: 10.1039/d5ra04275e

rsc.li/rsc-advances

Photocatalytic water splitting has emerged as a key approach to sustainable hydrogen production, yet many photocatalysts suffer from limited solar absorption and low conversion efficiency. In this study, we investigate the electronic, optical, and photocatalytic characteristics of $Sr_5Ta_4O_{15}$ through density functional theory (DFT) calculations, utilizing the generalized gradient approximation (GGA) for the exchange-correlation potential. The findings show that $Sr_5Ta_4O_{15}$ primarily absorbs ultraviolet (UV) light, which limits its photocatalytic activity to the UV range. To enhance its photocatalytic performance, we explore vanadium(v) doping in Tantalum (Ta) sites and the introduction of oxygen vacancies (OVs). The results demonstrate a significant improvement in photocatalytic performance, with hydrogen production rates increasing from 2.18 μmol g^{-1} for pure $Sr_5Ta_4O_{15}$ to 259.8 μmol g^{-1} for V-doped $Sr_5Ta_4O_{15}$ with oxygen defects. Furthermore, the quantum efficiency (QE) and solar-to-hydrogen (STH) conversion efficiency improve notably, with the STH efficiency reaching 17.1%. These modifications help overcome light-harvesting limitations and contribute valuable insights toward the development of more effective photocatalysts for solar-driven hydrogen production.

1. Introduction

Searching for efficient and sustainable energy solutions has led to an intense exploration of photocatalytic water splitting which is a crucial method in addressing energy and environmental challenges.[1–3] Since Fujishima and Honda's findings of water splitting using solar energy has emerged as a significant step to reinforce the performance.[4–9] Despite these advancements, industrial hydrogen is predominantly produced from fossil fuels due to the unbelievable cost of the existing photocatalytic systems.[10,11] The absence of durable photocatalysts operating under visible light with high efficiency remains a pivotal problem in commercializing photocatalytic water splitting.[12,13]

Solar energy has become a key player in the transition to renewable energy, powering technologies from photovoltaics and solar heating to artificial photosynthesis.[14] Among these innovations, photocatalysis stands out for its ability to convert sunlight into chemical energy using semiconductors that generate electron–hole pairs for redox reactions.[15–17] As the world grapples with rising energy demands and the environmental consequences of fossil fuels, solar-driven hydrogen production is emerging as a clean and sustainable solution.[3,8,18–20] However, realizing this potential depends on the development of advanced photocatalysts with the right band gaps and redox potentials to efficiently split water under sunlight.[21–24]

The critical pursuit of developing an extensive library of photocatalysts remains necessary for comprehending and designing highly active ones.[12] Therefore, tantalates have emerged as appropriate candidates for photocatalytic water splitting.[25–28]

The pursuit of efficient photocatalysts operating beyond ultraviolet (UV) irradiation has motivated researchers towards nitrogen-doped oxides, Tantalum (Ta)-based materials being of particular interest.[29–32] The exploration has led to the development of Ta-based photocatalysts that harness visible light for both water reduction and oxidation reactions.[32–35] Studies have examined $Sr_5Ta_4O_{15-x}N_x$, a nitrogen-doped Ta-based layered oxide synthesized *via* thermal ammonolysis.[36] When combined with optimized cocatalyst deposition and visible light irradiation, this photocatalyst demonstrated promising activity for both water reduction and oxidation, underscoring the potential of Ta-based layered oxides as visible-light-responsive materials for solar water splitting.[37] This research investigated the structural and electronic property modifications induced by nitrogen doping, contributing to a deeper understanding and broader application of these advanced materials.[36]

However, despite these advances, detailed insights into the intrinsic electronic structure of undoped $Sr_5Ta_4O_{15}$ remain limited. Most existing studies have focused on nitrogen doping or performance optimization, leaving the effects of other modifications, such as vanadium(v) doping and OVs, largely unexplored. Understanding how these specific changes

[a]*Laboratory of Condensed Matter and Interdisciplinary Sciences, Unité de Recherche Labellisée CNRST, URL-CNRST-17, Faculty of Sciences, Mohammed V University, Rabat, Morocco. E-mail: l.bahmad@um5r.ac.ma*

[b]*Hassan II Academy of Science and Technology, Rabat, Morocco*

influence the band structure and light absorption is essential for advancing visible-light-driven photocatalytic performance.

As for this current work, we selected the $Sr_5Ta_4O_{15}$ system as a photocatalyst for water splitting, aiming to explore the correlation between its photocatalytic capabilities and electronic properties with a particular emphasis on the band gap. This material has already been synthesized by using a polymerizable complex method as detailed in ref. 38 and 39. During this process, the system shows an appropriate thermal stability which results in the successful production of pure-phase $Sr_5Ta_4O_{15}$ at 1273 K in air for 60 hours. Despite the accomplishment, the crystal structure of $Sr_5Ta_4O_{15}$ remains undetermined.[39] A potential isostructural relationship with the known $Ba_5Ta_4O_{15}$ phase is supported by crystallographic studies reporting the formation of a (Sr, Ba)$_5Ta_4O_{15}$ solid solution.[37,39] Thus, the reaction involved the combination of $5SrCO_3$ with $4TaCl_5$, resulting in the formation of $Sr_5Ta_4O_{15}$ and $5CCl_4$.[37,39]

$$5SrCO_3 + 4TaCl_5 \rightarrow Sr_5Ta_4O_{15} + 5CCl_4 \quad (1)$$

By employing *ab initio* calculations, we thoroughly analyzed the structural geometry, electronic band structure and optical properties of powdered $Sr_5Ta_4O_{15}$. Additionally, we investigated the effect of V doping in $Sr_5Ta_4O_{15}$, focusing on its influence on the electronic properties and hydrogen yield. We also studied the role of oxygen defects in further modifying the electronic and photocatalytic behavior of both the undoped and V-doped material. Furthermore, Huang *et al.*[40] conducted a study on $Ba_5Ta_4O_{15}$, showing that under reduction conditions, significant OVs form and play a crucial role in enhancing catalytic activity. Their XPS analysis revealed an increase in OV concentration from 4% in the pristine state to 24% in Ru/$Ba_5Ta_4O_{15}$, and up to 63% in Cs–Ru/$Ba_5Ta_4O_{15}$. These results highlight the importance of OVs in facilitating surface reactions, thus supporting the theoretical exploration of such defects in $Sr_5Ta_4O_{15}$ at vacancy concentrations of 3.33% and 6.66%.

Our goal is to qualitatively estimate hydrogen production in photocatalysis based on pristine $Sr_5Ta_4O_{15}$ and its doped variants with V and OVs. To achieve this, we assume ideal conditions where all electrons in the valence band (VB) are excited under visible light, and no interactions with hydrogen occur at the surface states, allowing us to establish an order of hydrogen production.

This study aims to address the current lack of understanding regarding how structural modifications, specifically V doping and OVs, affect the electronic and optical behavior of $Sr_5Ta_4O_{15}$. By using first-principles calculations, we aim to provide insights that could guide the development of more efficient photocatalysts, particularly those capable of operating under visible light for sustainable hydrogen generation.

2. Computational details

The results of this study were derived using density functional theory (DFT) calculations performed with the Quantum ESPRESSO package.[41] The exchange–correlation energy was modeled using the generalized gradient approximation (GGA) with the Perdew–Burke–Ernzerhof (PBE) functional.[42] The electron–ion interactions were described using projector augmented-wave (PAW) pseudopotentials[43] for Sr ($5s^2$), Ta ($5d^36s^2$), and O ($2s^22p^4$). The electronic wave functions are expanded in *a* plane wave basis set with energy cut-offs (E_{cut}) of 1088 eV and charge density is taken 10 times of E_{cut}. For Brillouin-zone integration, a $7 \times 7 \times 3$ Monkhorst–Pack *k*-point grid was applied,[44] ensuring total energy convergence to a threshold of 10^{-5}.

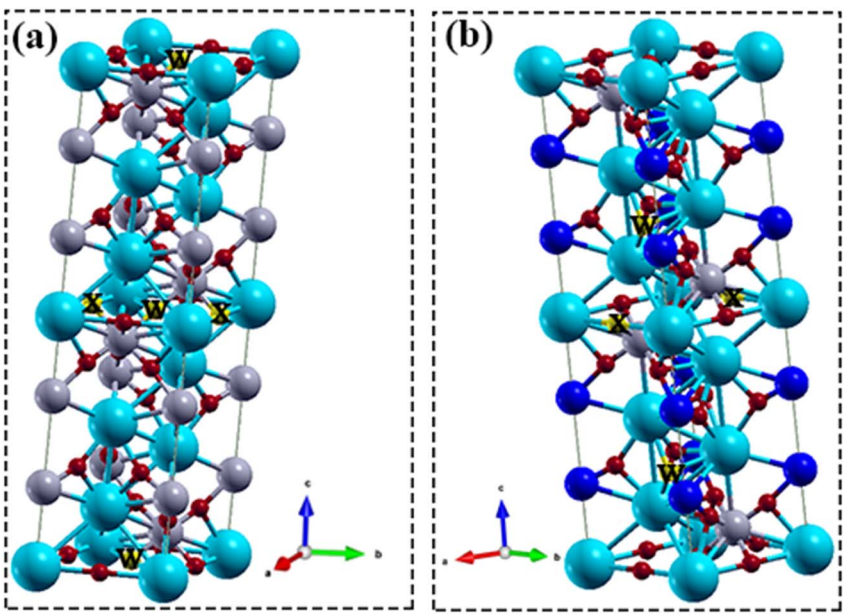

Fig. 1 Supercell $1 \times 1 \times 2$ showing (a) the crystal structure of $Sr_5Ta_4O_{15-\delta}$ and (b) the crystal structure of $Sr_5Ta_2V_2O_{15-\delta}$. The yellow spheres indicate the vacancy sites, with '*w*' representing $\delta = 6.66\%$ of vacancies and '*x*' representing $\delta = 3.33\%$ of vacancies.

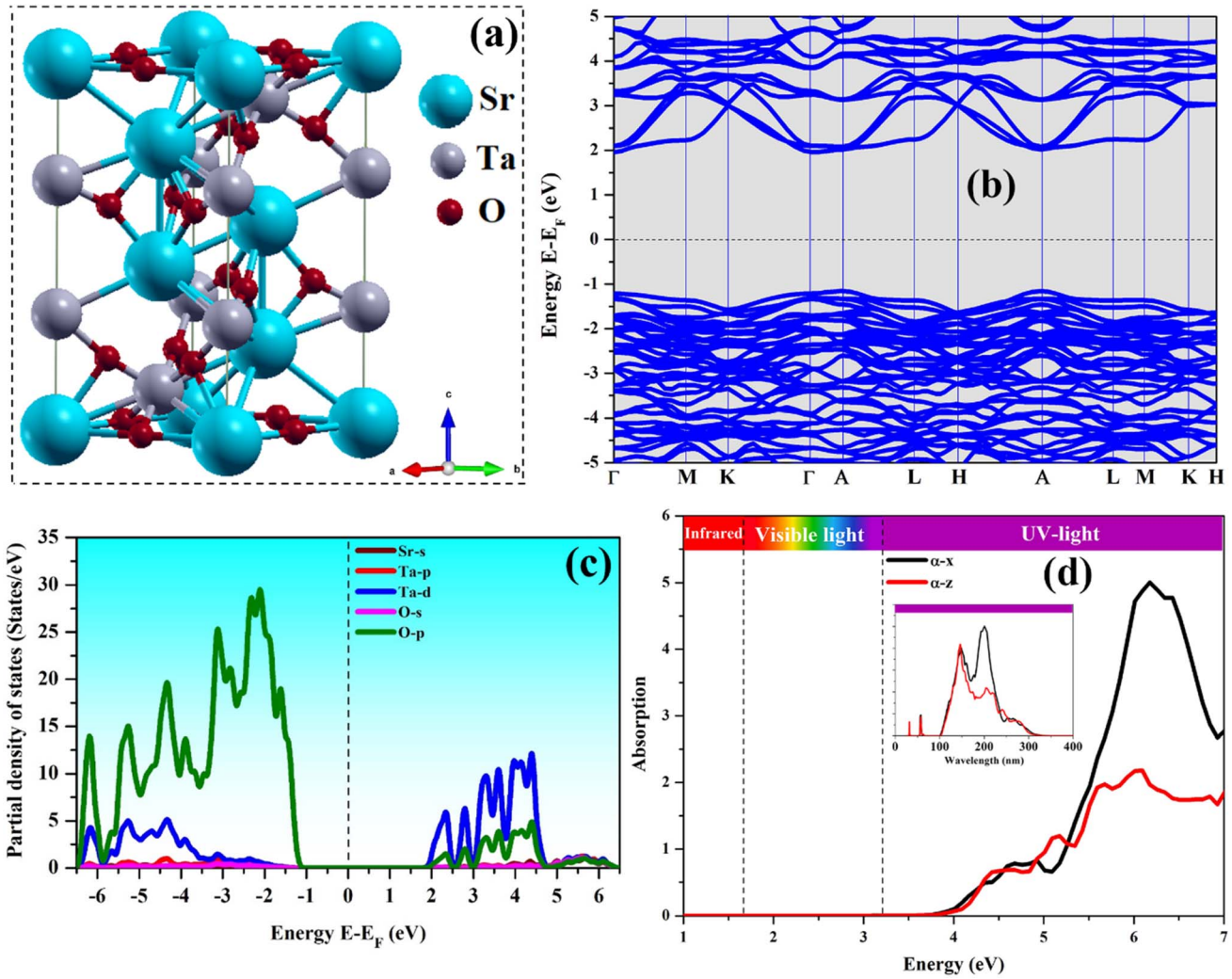

Fig. 2 (a) Crystal structure using Xcrysden code,[29] (b) band structure, (c) partial DOS and (d) absorption spectrum of $Sr_5Ta_4O_{15}$ as a function of photon energy.

For V doping and the introduction of OVs, we explored all possible configurations and selected the most stable ones based on their lowest optimized energies, as illustrated in Fig. 1:

The effective mass for both electrons and holes were evaluated through the equation:[45]

$$E(k) = E_0 + \frac{\hbar^2 k^2}{2m^*} \quad (2)$$

Here, $E(k)$ represents the energy of an electron at a specific wavevector k within the band, E_0 denotes the energy of free electrons on the hydrogen scale (0 V), and m^* refers to the effective mass, treated as a constant. The effective mass was calculated and expressed as m_0, the electron rest mass.

The valence and conduction band (CB) edges were computed by the following equations:

$$E_{CB}{}^0 = \chi(S) - E^0 - \frac{1}{2}E_g \quad (3)$$

$$E_{VB}{}^0 = E_{CB} + E_g \quad (4)$$

where $\chi(S)$ represents the Mulliken electronegativity of the semiconductor, $E_{VB}{}^0$, and $E_{CB}{}^0$ are the valence band maximum (VBM) and conduction band minimum (CBM), respectively, E_g is the band gap energy and E^0 is the scale factor relates the electrode redox potential to the absolute vacuum scale (AVS), typically $E^0 \sim 4.5$ eV for the normal hydrogen electrode (NHE).[46] The Mulliken electronegativity (χ) value for $Sr_5Ta_4O_{15}$, calculated using the Millikan approximation,[47–49] is 5.53 eV. This value was utilized to calculate the band edge potentials. The electronegativity $\chi(S)$ of a compound is computed using the following equation:

$$\chi(S) = \sqrt[N]{\chi_1^{Z_1}\chi_2^{Z_2}\chi_3^{Z_3}\ldots\ldots\ldots\chi_{n-1}^{Z_{n-1}}\chi_n^{Z_n}} \quad (5)$$

where N is the total number of atoms in the compound, $\chi_n{}^{Z_n}$ represents the electronegativity of the constituent atom, and Z_n is the number of atoms of that species. The electronegativity of an individual element, χ_i, is given by:

$$\chi_i(S) = \frac{E_i^{IE} + E_i^{AE}}{2} \quad (6)$$

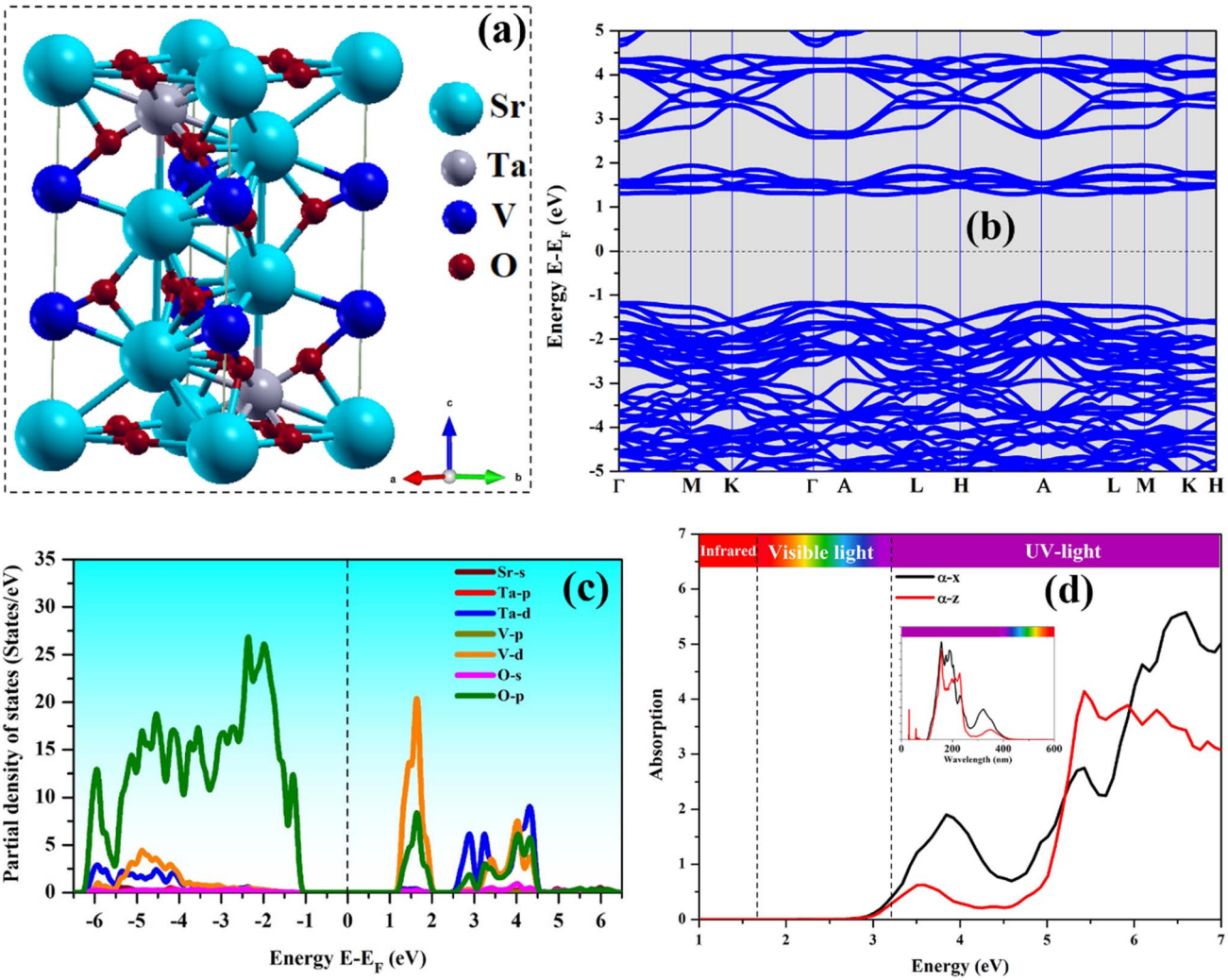

Fig. 3 (a) Crystal structure, (b) band structure, (c) partial DOS and (d) absorption spectrum of $Sr_5Ta_2V_2O_{15}$ as a function of photon energy.

Here, E_i^{IE} is the ionization energy, E_i^{AE} is the electron affinity energy and $\chi_i$is the electronegativity of the element.

The pH of solutions significantly influences the redox potential, affecting the conduction and VB edges. This relationship is expressed below as a function of pH:[50,51]

$$E_{CB}{}^{pH} = E_{CB}{}^{0} - 0.05911 \times (pH - pH_{pzc}) \quad (7)$$

$$E_{VB}{}^{pH} = E_{CB}{}^{pH} + E_g \quad (8)$$

where pH_{pzc} is the pH value at the point of zero charge ($pH_{pzc} = 0$).

3. Results and discussion

3.1 Structural, electronic and optical properties of pure $Sr_5Ta_4O_{15}$

$Sr_5Ta_4O_{15}$, crystallizes in a trigonal system, with space group $P\bar{3}m1$ as shown Fig. 2(a).[15] Using this structure, the initial lattice parameters were $a = 5.65$ Å and $c = 11.49$ Å.[37] After optimization, the lattice parameters were found to be $a = 5.69$ Å and $c = 11.62$ Å.

To gain insights into the optical properties, we analyzed the electronic properties by calculating the band structures (Fig. 2(b)) and the partial density of states (DOS) (Fig. 2(c)).

As shown in the DOS in Fig. S1, applying the GGA + U correction[52] slightly increases the band gap of pure $Sr_5Ta_5O_{15}$ from 3.11 eV to 3.22 eV, representing only a minor adjustment. Since the d orbitals of Ta are localized in the CB, the Hubbard correction is not expected to significantly affect the band gap value.

Fig. 2(b) shows that the VBM is located at the Γ point, and CBM is found at A point. This means that there is an indirect band gap and its value is 3.11 eV, in concordance with the previous reported value of 2.98 eV.[2]

To gain more insight into the electronic structure, we turn to the partial and total DOS shown in Fig. 2(c) and S2(a), respectively. The partial DOS (Fig. 2(c)) reveals that the contribution of the p orbital of the O anion is dominant near the VB with a very small contribution from the other orbitals of the Sr and Ta cations. On the other hand, near the CB, we can observe the dominance of the 5d orbital of Ta. This suggests that electronic

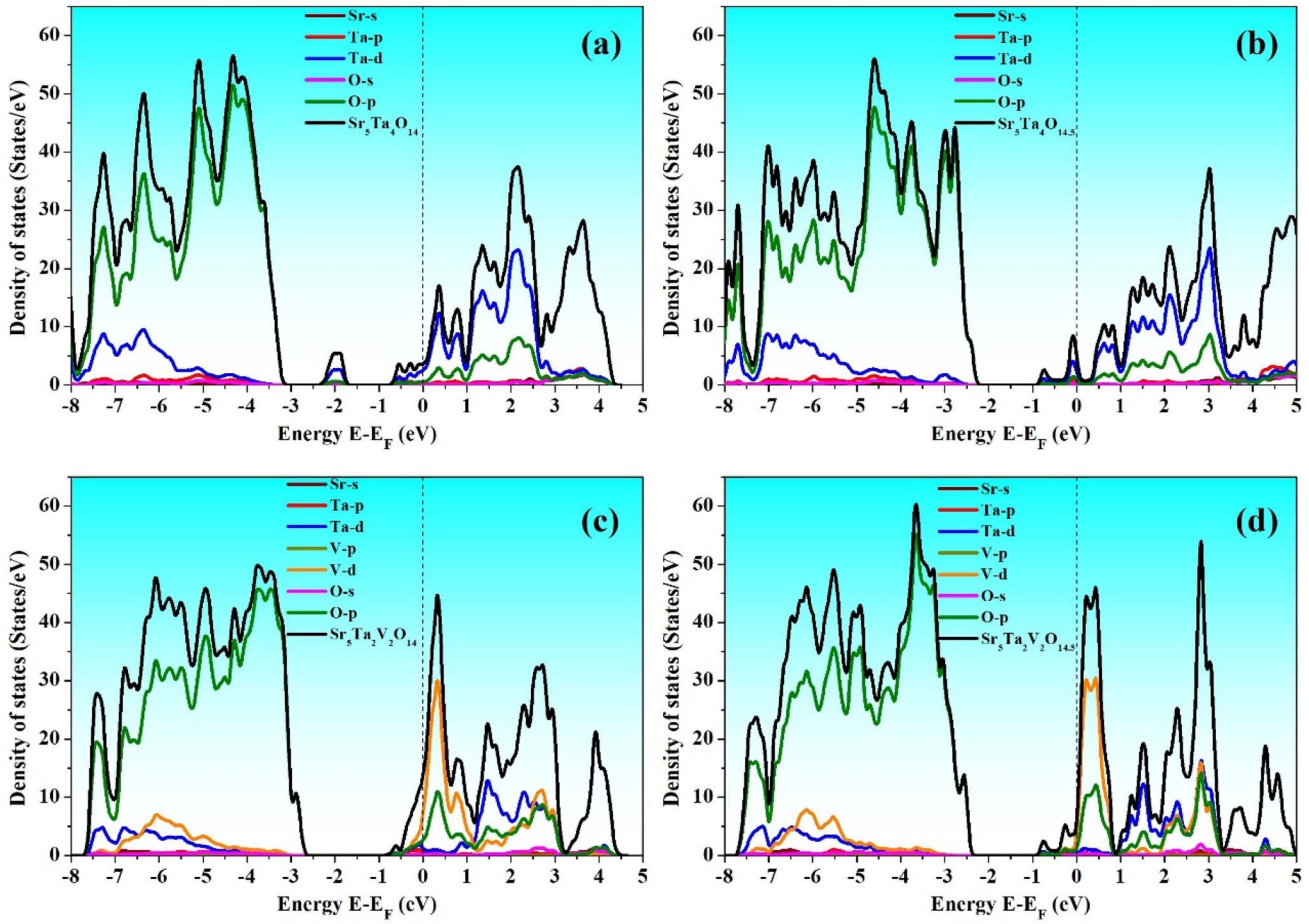

Fig. 4 DOS of (a) $Sr_5Ta_4O_{14}$, (b) $Sr_5Ta_4O_{14.5}$, (c) $Sr_5Ta_2V_2O_{14}$ and (d) $Sr_5Ta_2V_2O_{14.5}$.

transitions are likely to occur between O-2p and Ta-5d states, which is a common feature in tantalate-based oxides.[53,54]

The total DOS in Fig. S2(a) confirms the presence of a well-defined band gap, with no significant states within the gap region. The shape and position of the DOS curves reinforce the band structure findings and highlight the crucial role of Ta–O interactions in determining the material's semiconducting properties.

The optical responses of the $Sr_5Ta_4O_{15}$ phase are calculated for photon energies up to 10 eV. The real and imaginary parts of the dielectric function in relation to the absorption coefficient are presented in Fig. 2(d). The absorption coefficient "α" can be deliberated by the following term:[55]

$$\alpha(\omega) = 2\omega \times k(\omega) = \sqrt{2}\left[\left\{\varepsilon_1(\omega)^2 + \varepsilon_2(\omega)^2\right\}^{1/2} - \varepsilon_1(\omega)\right]^{1/2} \quad (9)$$

where ε_1 is the real part and ε_2 the imaginary part of the dielectric function.

The absorption spectrum demonstrates an absorbance in the UV range, accounting for only 5% of solar radiation. Also, it shows a first peak located at 4.6 eV, which corresponds to the optical gap $E_{\text{gopt}} = 3.98$ eV (see Fig. S3(a)). This value is slightly smaller than the experimentally reported optical gaps, which range from $E_{g_{\text{opt}}} = 4.51$ eV[36] to $E_{g_{\text{opt}}} = 4.75$ eV.[37] Whereas, the other peaks arise from transitions along the *K*, *Γ*, *L*, and *A* directions from the VB to the CB.

When light is polarized along the *x*- and *z*-axes, it generates two distinct spectra. This polarization-dependent behavior provides insight into the anisotropic properties of the material.

3.2 Vanadium substitution in $Sr_5Ta_4O_{15}$

Understanding the optical properties of a material is essential for its application. In this study, we investigate how V substitution at Ta sites affects the material's optical properties. The following sections present the results of our calculations, focusing on the changes in the DOS, band structure, and band gap induced by V doping.

Fig. 3(a) presents the structure obtained by substituting V at 50% of the Ta sites. After optimizing the cell parameters and atomic positions, we calculated the DOS and band structure.

The results, shown in Fig. 3(c) and S2(b), reveal clear changes in the electronic structure caused by V doping. The partial DOS in Fig. 3(c) shows that V-3d orbitals contribute significantly within the band gap region, especially just below the CB edge. This leads to the formation of mid-gap states, which are localized energy levels, were not present in the undoped material. These mid-gap features are also clearly visible in the total DOS

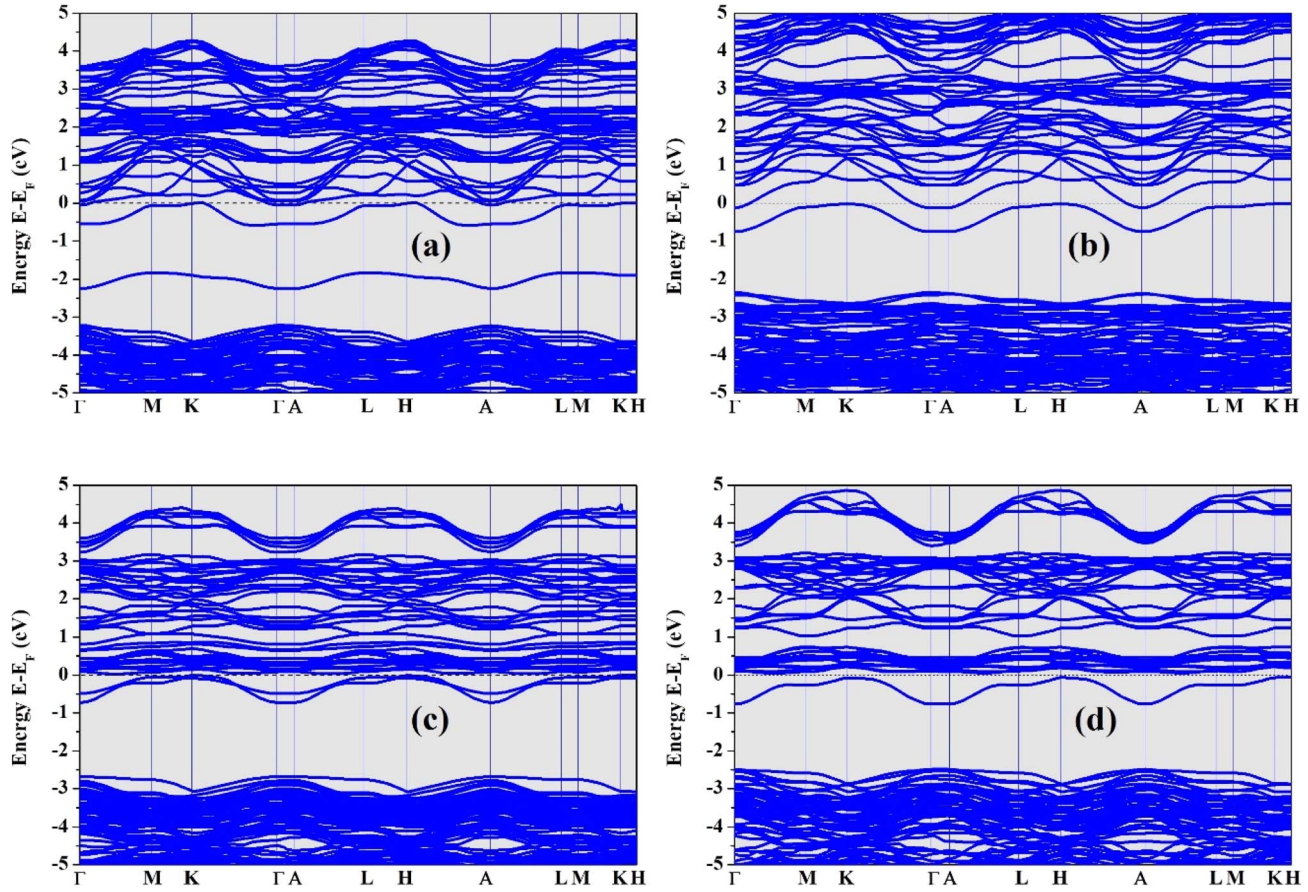

Fig. 5 Band structures of (a) $Sr_5Ta_4O_{14}$, (b) $Sr_5Ta_4O_{14.5}$, (c) $Sr_5Ta_2V_2O_{14}$ and (d) $Sr_5Ta_2V_2O_{14.5}$.

in Fig. S2(b), where the band gap is no longer clean and wide, but slightly filled by these new states.

These changes reduce the band gap from 2.98 eV in the pristine $Sr_5Ta_4O_{15}$ to 2.45 eV in the V-doped version. Fig. 3(b) confirms this reduction, showing an indirect band gap similar to the original structure.

The mid-gap states introduced by V slightly enhance light absorption near the visible-UV boundary, as illustrated in Fig. 3(d), indicating an improvement in optical properties due to doping. The optical gap decreases from a range of 2.97 eV to 3.05 eV ($E_{g_{opt}} = 2.97$ eV for lower energy transitions and $E_{g_{opt}} = 3.05$ eV for higher energy transitions, as shown in Fig. S3(b)),

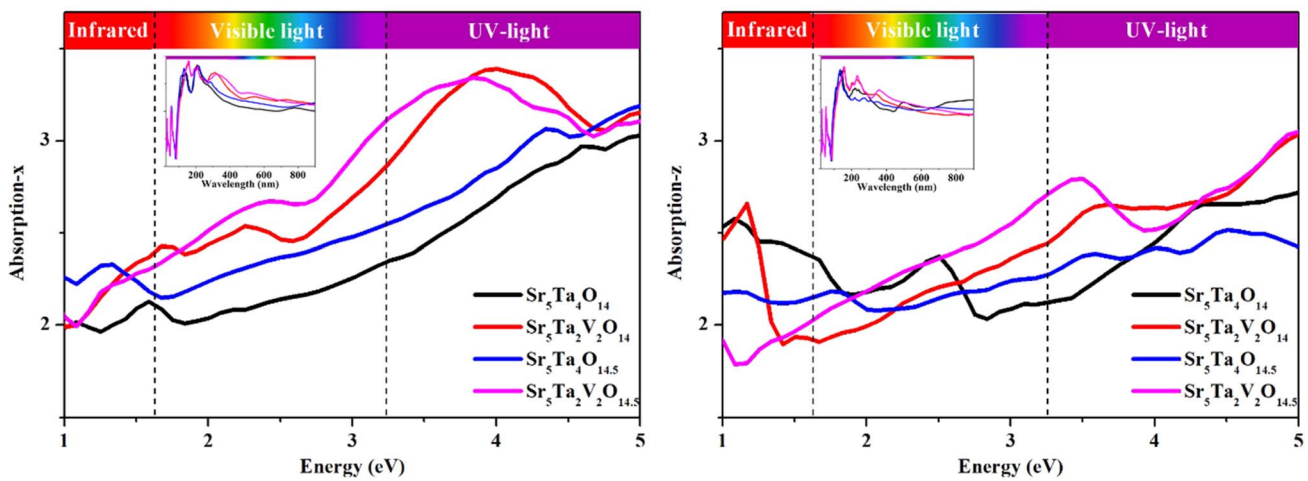

Fig. 6 Absorption spectrum of $Sr_5Ta_4O_{14}$, $Sr_5Ta_4O_{14.5}$, $Sr_5Ta_2V_2O_{14}$, and $Sr_5Ta_2V_2O_{14.5}$ as a function of photon energy.

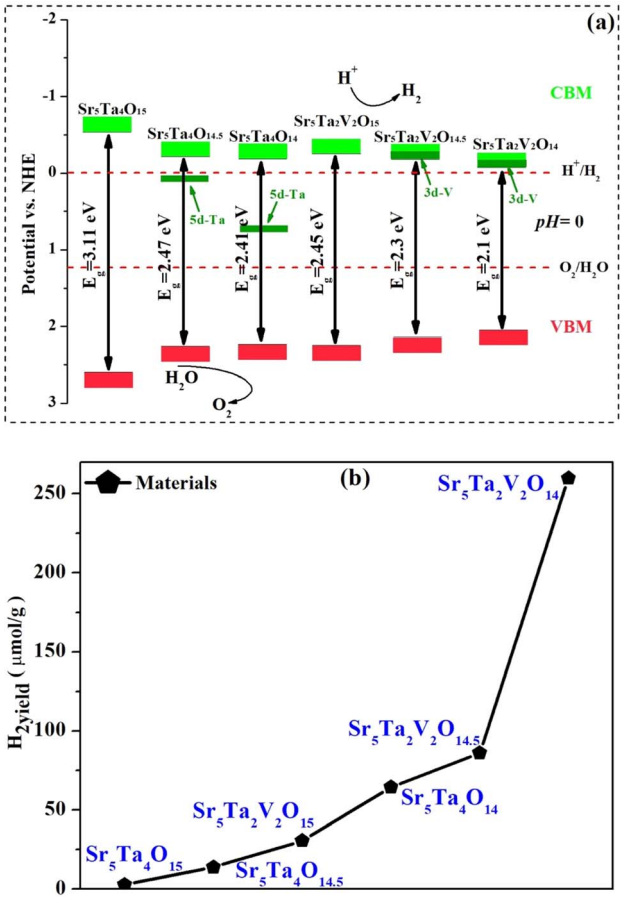

Fig. 7 (a) Band structures of $Sr_5Ta_4O_{15}$, $Sr_5Ta_4O_{14.5}$, $Sr_5Ta_4O_{14}$, $Sr_5Ta_2V_2O_{15}$, $Sr_5Ta_2V_2O_{14.5}$ and $Sr_5Ta_2V_2O_{14}$, photocatalysts, with red dashed lines representing the redox potentials of H^+/H_2 and O_2/H_2O. (b) Hydrogen yield analysis of the photocatalysts.

compared to the 3.98 eV gap of pure $Sr_5Ta_4O_{15}$. This reduction is attributed to the mid-gap states and crystal field splitting, which separates V d-orbitals into partially filled t_{2g} and e_g states. Transitions between t_{2g} and e_g levels occur, with the lowest energy transition at 2.85 eV. This change in the optical gap made by this material retains the same anisotropic properties as the pure $Sr_5Ta_4O_{15}$ when light is polarized along the *x*- and *z*-axes.

3.3 Effect of oxygen vacancies

The electronic properties of $Sr_5Ta_4O_{15}$, along with its V-doped variant, $Sr_5Ta_2V_2O_{15}$, can be significantly modified by introducing OVs. These vacancies create defect states within the material's band structure, altering its electronic behavior. In particular, OVs act as electron donors, which can boost conductivity and improve overall electronic performance.

To reduce the concentration of OVs, we created a supercell with dimensions $1 \times 1 \times 2$, which helps to control the vacancy density more effectively. For $Sr_5Ta_4O_{15}$ (Fig. 4(a) and (b)), OVs at concentrations of 6.66% ($Sr_5Ta_4O_{14}$) and 3.33% ($Sr_5Ta_4O_{14.5}$) lead to the formation of mid-gap states associated with Ta 5-d orbitals. These mid-gap states, located near the Fermi level, facilitate electron excitation from the VB to CB. When OVs are combined with V doping (Fig. 4(c) and (d)), the band gap is further reduced. Donor states introduced by the 3d orbitals of V lower the energy gap between the valence and conduction bands, improving light absorption and electron–hole pair generation for photocatalytic reactions. The DOS (Fig. 4) and band structure (Fig. 5) illustrate the narrowing of the band gap, which enables the material to absorb a wider spectrum of light.

Additionally, Fig. 6 highlights the synergistic effect of doping and OVs on absorption enhancement. The absorption spectra reveal a substantial increase in absorption intensity in both the visible and UV regions for materials exhibiting combined doping and defects. This enhancement is attributed to the interaction of mid-gap states and donor states, which together create additional pathways for light-induced electron transitions. The material also retains its anisotropic optical properties, as evidenced by polarization-dependent absorption along the *x*- and *z*-axes.

To gain deeper insight into the electronic impact of OVs, we performed Bader charge[56] analysis to examine how charge is redistributed around the defect sites. Our results show a noticeable decrease in Bader charge on the Ta atoms that were originally bonded to the missing oxygen atom. In the pristine $Sr_5Ta_4O_{15}$ structure, Ta atoms typically exhibit a Bader charge of about $+2.83e$, while the oxygen atom carries a charge of approximately $-1.31e$. When an oxygen atom is removed (creating $Sr_5Ta_4O_{14}$), its charge is primarily redistributed onto the neighboring Ta atoms, with a smaller portion spreading to adjacent atoms.

In the V-doped structure ($Sr_5Ta_2V_2O_{15}$), when an oxygen atom is removed, forming $Sr_5Ta_2V_2O_{14}$, the vacancy region retains a Bader charge of approximately $-1.07e$, indicating that a significant amount of electron density remains localized near the defect site. This excess charge is primarily transferred to the adjacent V atom, whose Bader charge decreases from $+2.20e$ in $Sr_5Ta_2V_2O_{15}$ to $+1.78e$ in $Sr_5Ta_2V_2O_{14}$, reflecting a notable gain in electron density. The rest of the redistributed charge is shared among neighboring atoms.

This behavior highlights the donor-like nature of OVs, which introduce localized states within the band gap. These states facilitate effective charge separation and suppress electron–hole recombination, key factors in enhancing photocatalytic performance.

3.4 Photocatalytic properties

For efficient water splitting in a semiconductor photocatalyst, the band gap energy (E_g) should exceed 1.23 eV. Additionally, the CB edge must be positioned above the water reduction level (H^+/H_2) at 0 V *vs.* NHE, while the VB edge should lie below the water oxidation level (O_2/H_2O) at 1.23 V *vs.* NHE. When illuminated with photons of energy equal to or greater than the semiconductor photocatalyst's band gap energy, electrons move from the VB to the CB by creating holes in the VB. Subsequently, the electrons reduce H^+ to H_2, while the holes simultaneously oxidize H_2O to H^+ and O_2, resulting in overall water splitting.

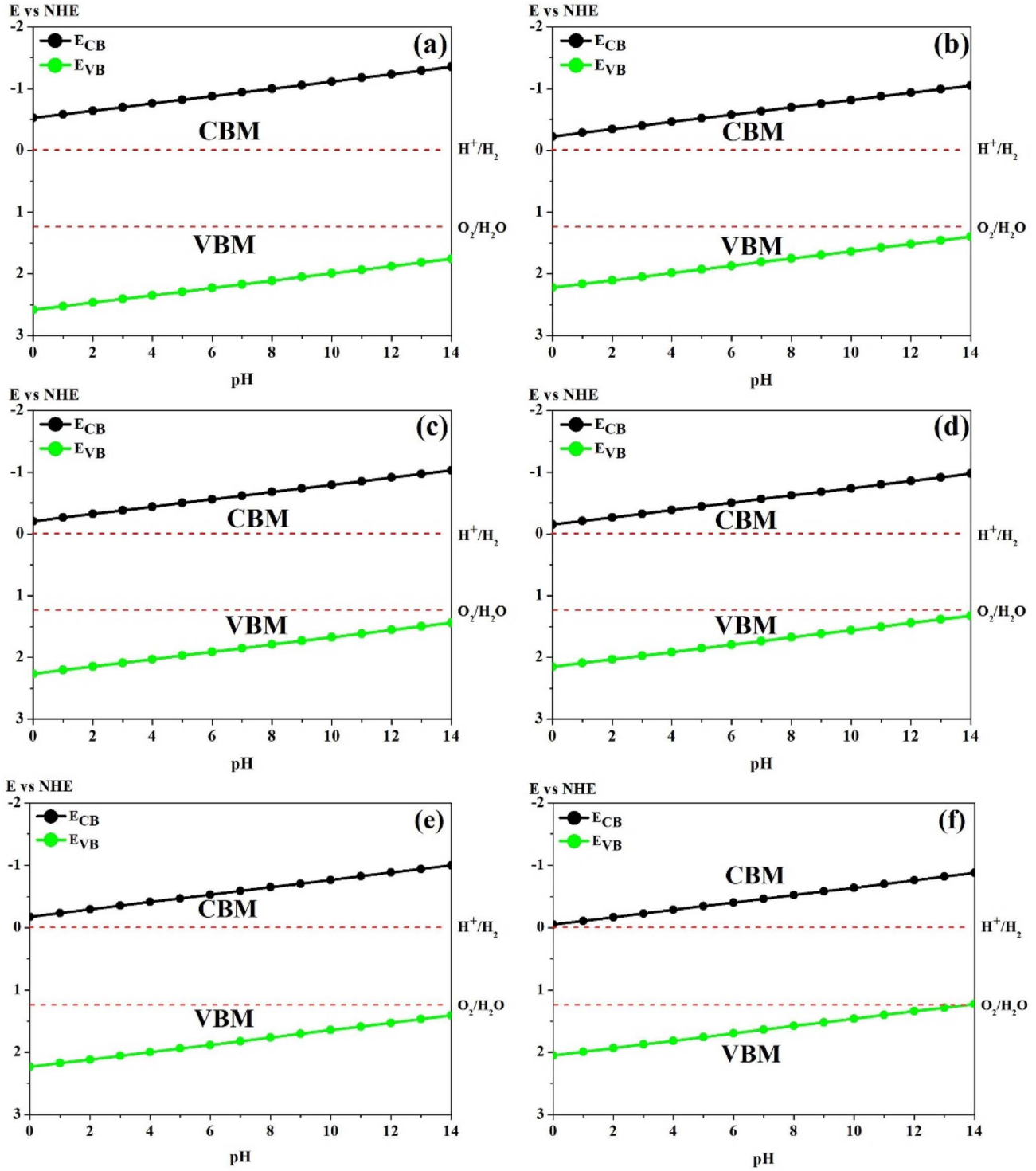

Fig. 8 Band edges as a function of pH for (a) $Sr_5Ta_4O_{15}$, (b) $Sr_5Ta_2V_2O_{15}$, (c) $Sr_5Ta_4O_{14.5}$, (d) $Sr_5Ta_2V_2O_{14.5}$, (e) $Sr_5Ta_4O_{14}$ and (f) $Sr_5Ta_2V_2O_{14}$.

To verify these criteria, we calculated the potentials of the CBM and VBM for The $Sr_5Ta_4O_{15}$ material using formulas (3) and (4).

The calculated CBM and VBM potentials of $Sr_5Ta_4O_{15}$ are displayed in Fig. 7(a).

The VBM of $Sr_5Ta_4O_{15}$ is higher than the oxidation potential of O_2/H_2O (+1.23 V *vs.* NHE), indicating that the photogenerated holes (h^+) possess sufficient oxidative power to drive water oxidation and produce oxygen, as described by the equation:

$$H_2O + 2h^+ \rightarrow 2H^+ + \frac{1}{2}O_2 \quad (10)$$

Table 1 Calculated band edge offsets ($\Delta\chi$) of VBM and CBM for $Sr_5Ta_4O_{15}$ systems with V-doping and OVs

System	$\Delta\chi$ VBM (eV)	$\Delta\chi$ CBM (eV)
$Sr_5Ta_4O_{14.5}$	1.85	−0.62
$Sr_5Ta_4O_{14}$	1.82	−0.59
$Sr_5Ta_2V_2O_{14.5}$	1.73	−0.56
$Sr_5Ta_2V_2O_{14}$	1.63	−0.46

The CBM lies approximately 0.525 eV below the H^+/H_2 reduction potential (0 V *vs.* NHE), suggesting that the photogenerated electrons (e^-) have adequate reduction potential to reduce protons and generate hydrogen, as represented by the formula:

$$2H^+ + 2e^- \rightarrow H_2 \quad (11)$$

The simultaneous reduction of H^+ and oxidation of H_2O prevents hole accumulation in the VB, thus minimizing undesired recombination between e^- and h^+.

The CBM and VBM potentials for the V-doped and oxygen-vacancy-modified structures are shown in Fig. 7(a). In these materials, h^+ remain below the O_2/H_2O redox potential, while e^- are positioned above the H^+/H_2 reduction potential. The band gap values are 3.11 eV, 2.47 eV, 2.41 eV, 2.45 eV, 2.3 eV, and 2.1 eV for $Sr_5Ta_4O_{15}$, $Sr_5Ta_4O_{14.5}$, $Sr_5Ta_4O_{14}$, $Sr_5Ta_2V_2O_{15}$, $Sr_5Ta_2V_2O_{14.5}$, and $Sr_5Ta_2V_2O_{14}$, respectively. In agreement with recent mechanistic models,[57] the positioning of the conduction and valence bands in V-doped $Sr_5Ta_4O_{15}$ suggests that photogenerated electrons and holes possess sufficient potential for H_2 and O_2 evolution, respectively.

Surface states introduced by OVs and V doping are positioned closer to the H^+/H_2 reduction potential, except for $Sr_5Ta_4O_{14.5}$ and $Sr_5Ta_4O_{14}$, where these states are located below the H^+/H_2 reduction potential. These observations indicate that materials doped with V and modified by OVs have a greater potential to produce hydrogen compared to pure $Sr_5Ta_4O_{15}$ (see Fig. 7(b))[58,59]

Fig. 8 shows the evolution of the CBM and VBM positions of pristine $Sr_5Ta_4O_{15}$, its V-doped variant, and structures containing OVs as a function of pH, compared with the redox potentials relevant to water splitting.

In Fig. 8(a), the pristine $Sr_5Ta_4O_{15}$ exhibits band edges well aligned with the H^+/H_2 and O_2/H_2O redox levels across a broad pH range. Fig. 8(b) demonstrates that V doping preserves this favorable alignment, with both CBM and VBM remaining suitably positioned to drive hydrogen and oxygen evolution. Fig. 8(c)–(f) highlight the effects of introducing OVs and additional V doping. Although the band edges shift slightly in these modified structures, they continue to straddle the water redox levels, particularly near neutral pH (6–8). The calculated band edge offsets are presented in Table 1.

These values confirm that photogenerated electrons and holes in all studied structures retain sufficient redox potential to drive H_2 and O_2 evolution.

Under acidic conditions (low pH), the driving force for hydrogen evolution diminishes slightly as the CBM approaches the H^+/H_2 level. In contrast, near-neutral pH provides a better balance between band alignment and redox potentials, supporting optimal photocatalytic performance.

Overall, pristine $Sr_5Ta_4O_{15}$, V-doped variants, and OV-containing structures all maintain suitable band positions for water splitting across a wide pH range. Nonetheless, near-neutral or mildly basic conditions are most favorable, offering sufficient kinetic driving force while minimizing band misalignment and charge-recombination losses.[18,60,61]

The hydrogen production rates for the materials are presented in Fig. 7(b) and Table 2. A significant improvement is observed compared to the undoped material. This enhancement is attributed to mid-gap states introduced by V doping, where the 3d orbitals of V and 5d orbitals of Ta act as donor levels. These donor levels facilitate electron transfer to the CB, improving charge separation and reducing recombination rates.

These findings demonstrate that V doping and OVs significantly enhance the photocatalytic performance of $Sr_5Ta_2V_2O_{15}$, making it a promising material for hydrogen production.

For the quantum efficiency (QE), we use the following equation:[62]

$$QE = (1 - R(E)) \times (1 - e^{-\alpha(E)t}) \quad (12)$$

where $R(E)$ is the reflectivity, $\alpha(E)$ is the absorption, and the sample thickness t is set to 500 nm.[63] The QE measures how efficiently the material uses light at different energies. The Fig. 9(a) shows that the pure $Sr_5Ta_4O_{15}$ material has low QE, indicating it is transparent to light at lower energies. After doping with V and introducing OVs, new defect states are created, which improve the material's ability to absorb light, increasing the QE.

Table 2 Effective mass values, concentration of electrons, and hydrogen yield

	Effective mass of electron (m_0)	Effective mass of hole (m_0)	Concentration of electrons	H_2 yield
$Sr_5Ta_4O_{15}$	0.97	1.87	2.39×10^{19} cm^{-3}	2.85 μmol g^{-1}
$Sr_5Ta_4O_{14,5}$	1.17	1.41	3.16×10^{19} cm^{-3}	13.8 μmol g^{-1}
$Sr_5Ta_4O_{14}$	2.82	5.67	1.18×10^{20} cm^{-3}	64.4 μmol g^{-1}
$Sr_5Ta_2V_2O_{15}$	4.19	1.86	5.69×10^{19} cm^{-3}	30.6 μmol g^{-1}
$Sr_5Ta_2V_2O_{14,5}$	3.08	2.20	2.14×10^{20} cm^{-3}	86.07 μmol g^{-1}
$Sr_5Ta_2V_2O_{14}$	6.34	2.83	3.99×10^{20} cm^{-3}	259.8 μmol g^{-1}

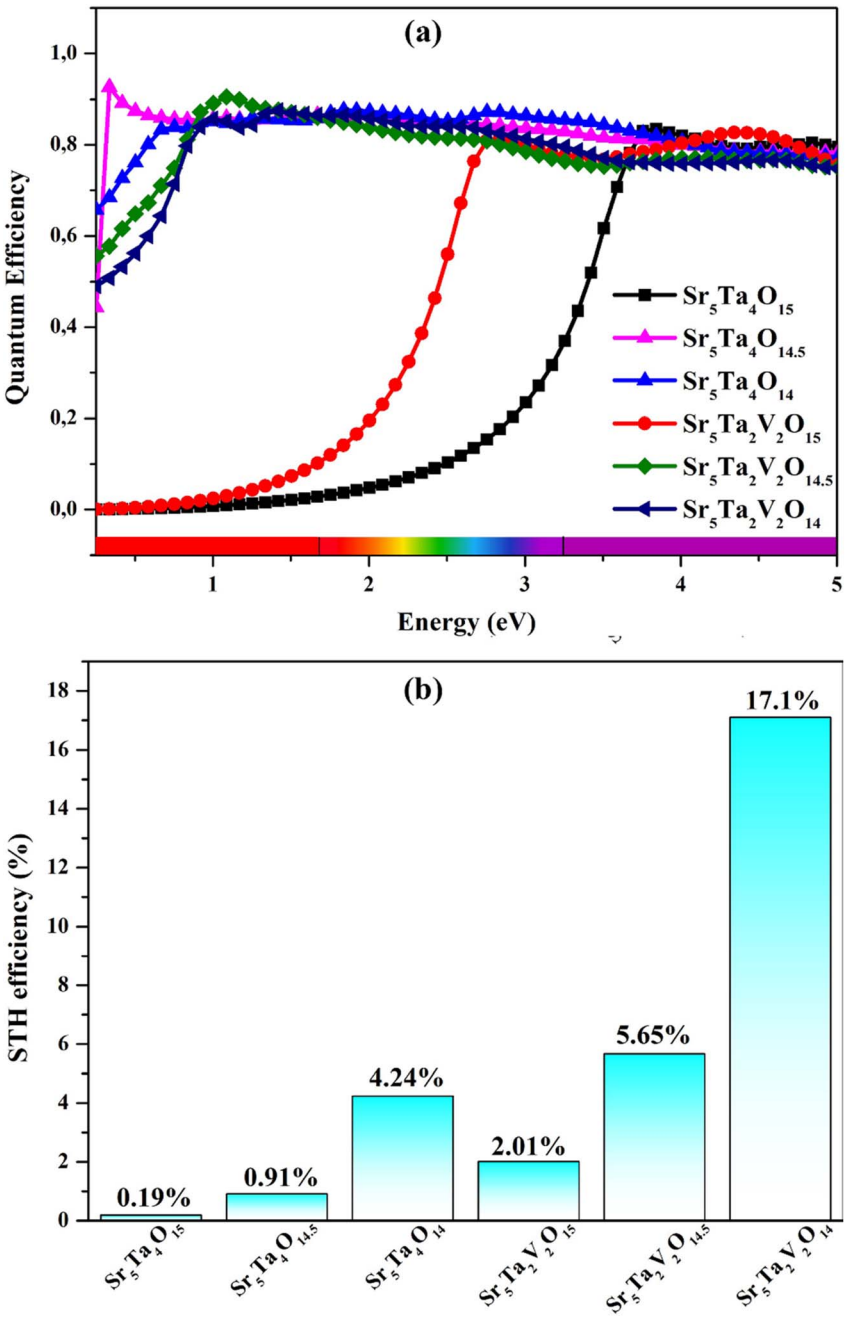

Fig. 9 (a) QE and (b) STH efficiency of $Sr_5Ta_4O_{15}$: effects of doping and OVs.

The solar-to-hydrogen (STH) efficiency was determined using the following formula:[64]

$$\mathrm{STH}(\%) = \frac{r_{H_2} \times \Delta G}{P_{\mathrm{light}} \times S} \times 100 \quad (13)$$

where r_{H_2} is the hydrogen evolution rate (H_2 yield), ΔG is the Gibbs free energy for water splitting, Pl_{ight} is the solar power input, and S is the irradiation area. For our calculations, we assume standard 1-sun (AM 1.5G) conditions with a light intensity of 1000 W m^{-2} and assume the QE at its maximum value. Based on these conditions, we estimate a theoretical upper limit for the STH efficiency, as shown in Fig. 9(b). Our findings also shows that $Sr_5Ta_2V_2O_{14}$ stands out with an impressive STH efficiency of 17.1%, compared to only 0.19% for the undoped $Sr_5Ta_4O_{15}$.

To highlight the performance of our V-doped $Sr_5Ta_4O_{15}$ system with OVs, we compared it with other promising photocatalysts in terms of hydrogen production and STH efficiency, as shown in Table 3. Our system outperforms widely studied oxide photocatalysts such as CeO_2 (32 μmol g^{-1})[65] and N-/Br-doped TiO_2 (4.4–5.2 μmol g^{-1}),[66] demonstrating the strong impact of V doping and OV engineering in enhancing photocatalytic activity. This performance also rivals that of BiAgOS (289.56

Table 3 Comparison of H_2 yield and STH efficiencies of V-doped $Sr_5Ta_4O_{15}$ with OVs and other reported photocatalysts

Systems	H_2 yield	STH	References
$Sr_5Ta_4O_{15}$	2.85 μmol g^{-1}	0.19%	This work
$Sr_5Ta_4O_{14}$	64.4 μmol g^{-1}	4.24%	This work
$Sr_5Ta_2V_2O_{15}$	30.6 μmol g^{-1}	2.01%	This work
$Sr_5Ta_2V_2O_{14}$	259.8 μmol g^{-1}	17.1%	This work
CeO_2	32 μmol g^{-1}	—	65
N–TiO_2	4.4 μmol g^{-1}	—	66
Br–TiO_2	5.2 μmol g^{-1}	—	66
$MAPbI_3$	150 μmol g^{-1}	—	18
BiAgOS	289.56 μmol g^{-1}	19.06%	17
$CsGeCl_2I$ (−6% strain)	—	14.60%	67
InP (2D) (+6% strain)	15.96 μmol g^{-1}	—	68

μmol g^{-1}, 19.06%)[17] and surpasses those of strained $CsGeCl_3$,[67] 2D InP,[68] and $MAPbI_3$ (150 μmol g^{-1}).[18]

4. Conclusion

In conclusion, we opted the DFT method within the Quantum ESPRESSO package, employing the GGA approximation to examine the structural, electronic, and optical properties of $Sr_5Ta_4O_{15}$. Hence, the outcomes demonstrate that $Sr_5Ta_4O_{15}$ is a semiconductor with a 3.11 eV band gap and absorbs light in the UV range. The introduction of OVs in $Sr_5Ta_4O_{15}$ and its V-doped form, $Sr_5Ta_2V_2O_{15}$, significantly improves its electronic properties and enhances hydrogen production efficiency. OVs act as electron donors, increasing CB electron density and promoting charge separation. Notably, V doping reduces the band gap of $Sr_5Ta_2V_2O_{15}$ to 2.45 eV, enhancing charge carrier generation. These findings highlight $Sr_5Ta_4O_{15}$, with optimized OVs and V doping, as promising candidates for photocatalytic hydrogen generation. Further material optimization could accelerate the development of efficient, sustainable photocatalytic systems for renewable energy applications. To strengthen the validity of our results, we propose validating the theoretical findings by comparing them with experimental measurements of the material's optical and photocatalytic properties. This will provide a more comprehensive understanding of the material's behavior and further support the accuracy of our computational results.

Author contributions

Ahmed Brach: writing – original draft, software, methodology, investigation, conceptualization. Halima Zaari: writing – review & editing, visualization, validation, software, investigation. Abdelilah Benyoussef: writing – review & editing, validation, methodology, investigation. Lahoucine Bahmad: validation, supervision.

Conflicts of interest

The authors declare that they have no known competing financial interests or personal relationships that could have appeared to influence the work reported in this paper.

Data availability

The computational data supporting the findings of this study, including input files and optimized structures of $Sr_5Ta_4O_{15}$ and its doped/defective variants, are available from the corresponding author upon reasonable request.

Supplementary information is available and includes density of states (DOS) plots for $Sr_5Ta_4O_{15}$ and $Sr_5Ta_2V_2O_{15}$, as well as optical band gap determinations using absorption spectra analysis. See DOI: https://doi.org/10.1039/d5ra04275e.

Acknowledgements

The authors acknowledge that all results within this research project was supported by Laboratorio Nacional de Supercómputo del Sureste de México (LNS), a member of CONACYT national laboratories, for the computational resources provided through project n° 202403063n, And computational resources of HPC-MARWAN (hpc.marwan.ma) provided by the National Center for Scientific and Technical Research (CNRST), Rabat, Morocco.

References

1 K. Maeda, et al., Photocatalyst releasing hydrogen from water, *Nature*, 2006, **440**(7082), 295, DOI: 10.1038/440295A.
2 S. Y. Reece, et al., Wireless solar water splitting using silicon-based semiconductors and earth-abundant catalysts, *Science*, 2011, **334**(6056), 645–648, DOI: 10.1126/SCIENCE.1209816.
3 S. Huang, et al., Surface electrical properties modulation by multimode polarizations inside hybrid perovskite films investigated through contact electrification effect, *Nano Energy*, 2021, **89**, 106318, DOI: 10.1016/J.NANOEN.2021.106318.
4 A. Fujishima and K. Honda, Electrochemical photolysis of water at a semiconductor electrode, *Nature*, 1972, **238**(5358), 37–38, DOI: 10.1038/238037A0.
5 Y. Tachibana, L. Vayssieres and J. R. Durrant, Artificial photosynthesis for solar water-splitting, *Nat. Photonics*, 2012, **6**(8), 511–518, DOI: 10.1038/NPHOTON.2012.175.
6 K. Sayama, K. Mukasa, R. Abe, Y. Abe and H. Arakawa, A new photocatalytic water splitting system under visible light irradiation mimicking a Z-scheme mechanism in photosynthesis, *J. Photochem. Photobiol. A Chem.*, 2002, **148**(1–3), 71–77, DOI: 10.1016/S1010-6030(02)00070-9.
7 H. Kato, M. Hori, R. Konta, Y. Shimodaira and A. Kudo, Construction of Z-scheme type heterogeneous photocatalysis systems for water splitting into H_2 and O_2 under visible light irradiation, *Chem. Lett.*, 2004, **33**(10), 1348–1349, DOI: 10.1246/CL.2004.1348.
8 O. Mounkachi, et al., Stability, electronic structure and thermodynamic properties of nanostructured MgH_2 thin films, *Energies*, 2021, **14**(22), 7737, DOI: 10.3390/EN14227737.
9 J. Yang, D. Wang, H. Han and C. Li, Roles of cocatalysts in photocatalysis and photoelectrocatalysis, *Acc. Chem. Res.*, 2013, **46**(8), 1900–1909.

10 K. H. Ng, S. Y. Lai, C. K. Cheng, Y. W. Cheng and C. C. Chong, Photocatalytic water splitting for solving energy crisis: myth, fact or busted?, *Chem. Eng. J.*, 2021, **417**, 128847, DOI: 10.1016/J.CEJ.2021.128847.

11 A. Kudo and Y. Miseki, Heterogeneous photocatalyst materials for water splitting, *Chem. Soc. Rev.*, 2008, **38**(1), 253–278, DOI: 10.1039/B800489G.

12 Z. Kuspanov, B. Bakbolat, A. Baimenov, A. Issadykov, M. Yeleuov and C. Daulbayev, Photocatalysts for a sustainable future: Innovations in large-scale environmental and energy applications, *Sci. Total Environ.*, 2023, **885**, 163914, DOI: 10.1016/J.SCITOTENV.2023.163914.

13 X. Zhang, X. Zhao, D. Wu, Y. Jing and Z. Zhou, MnPSe3 monolayer: a promising 2D visible-light photohydrolytic catalyst with high carrier mobility, *Adv. Sci.*, 2016, **3**(10), 1600062, DOI: 10.1002/ADVS.201600062.

14 Y. Fu, Y. Wang, J. Huang, K. Lu and M. Liu, Solar fuel production through concentrating light irradiation, *Green Energy Environ.*, 2024, **9**(10), 1550–1580, DOI: 10.1016/J.GEE.2024.01.001.

15 Y. Li, C. Gao, R. Long and Y. Xiong, Photocatalyst design based on two-dimensional materials, *Mater. Today Chem.*, 2019, **11**, 197–216, DOI: 10.1016/J.MTCHEM.2018.11.002.

16 Y. X. Leiu, G. Z. S. Ling, A. R. Mohamed, S. Wang and W. J. Ong, Atomic-level tailoring ZnxCd$_{1-x}$S photocatalysts: a paradigm for bridging structure-performance relationship toward solar chemical production, *Mater Today Energy*, 2023, **34**, 101281, DOI: 10.1016/J.MTENER.2023.101281.

17 O. Ben Abdelhadi, et al., Unveiling the photocatalytic potential of BiAgOS solid solution for hydrogen evolution reaction, *Nanomaterials*, 2024, **14**(23), 1869, DOI: 10.3390/NANO14231869.

18 A. Al-Shami, et al., Photocatalytic properties of ZnO:Al/MAPbI$_3$/Fe$_2$O$_3$ heterostructure: first-principles calculations, *Int. J. Mol. Sci.*, 2023, **24**(5), 4856, DOI: 10.3390/IJMS24054856/S1.

19 X. Zhu, Y. Lin, Y. Sun, M. C. Beard and Y. Yan, Lead-halide perovskites for photocatalytic α-alkylation of aldehydes, *J. Am. Chem. Soc.*, 2019, **141**(2), 733–738, DOI: 10.1021/JACS.8B08720.

20 G. Liang, et al., Enhanced photocatalytic hydrogen evolution under visible light irradiation by p-type MoS$_2$/n-type Ni$_2$P doped g-C$_3$N$_4$, *Appl. Surf. Sci.*, 2020, **504**, 144448, DOI: 10.1016/J.APSUSC.2019.144448.

21 N. Rahamathulla and A. P. Murthy, Advanced heterostructures as bifunctional electrocatalysts for overall water splitting – a review, *J. Energy Storage*, 2023, **73**, 109127, DOI: 10.1016/J.EST.2023.109127.

22 Z. Kerrami, A. Sibari, O. Mounkachi, A. Benyoussef and M. Benaissa, Improved photo-electrochemical properties of strained SnO$_2$, *Int. J. Hydrogen Energy*, 2020, **45**(19), 11035–11039, DOI: 10.1016/J.IJHYDENE.2018.03.199.

23 A. U. Orozco-Valencia, J. L. Gázquez and A. Vela, Global and local partitioning of the charge transferred in the parr-pearson model, *J. Phys. Chem. A*, 2017, **121**(20), 4019–4029, DOI: 10.1021/ACS.JPCA.7B01765.

24 B. Samanta, et al., Challenges of modeling nanostructured materials for photocatalytic water splitting, *Chem. Soc. Rev.*, 2022, **51**(9), 3794–3818, DOI: 10.1039/D1CS00648G.

25 H. Kato and A. Kudo, Photocatalytic water splitting into H$_2$ and O$_2$ over various tantalate photocatalysts, *Catal. Today*, 2003, **78**(1–4), 561–569, DOI: 10.1016/S0920-5861(02)00355-3.

26 A. Kudo, H. Kato and S. Nakagawa, Water splitting into H$_2$ and O$_2$ on new Sr$_2$M$_2$O$_7$ (M = Nb and Ta) photocatalysts with layered perovskite structures: factors affecting the photocatalytic activity, *J. Phys. Chem. B*, 1999, **104**(3), 571–575, DOI: 10.1021/JP9919056.

27 M. Machida, J. I. Yabunaka and T. Kijima, Synthesis and photocatalytic property of layered perovskite tantalates, RbLnTa$_2$O$_7$ (Ln = La, Pr, Nd, and Sm), *Chem. Mater.*, 2000, **12**(3), 812–817, DOI: 10.1021/CM990577J.

28 F. Mezzat, H. Zaari, A. El Kenz and A. Benyoussef, Enhanced visible light photocatalytic activity of KTaO$_3$ (Se,V): DFT investigation, *Comput. Condens. Matter*, 2022, **30**, e00648, DOI: 10.1016/J.COCOM.2022.E00648.

29 G. Hitoki, T. Takata, J. N. Kondo, M. Hara, H. Kobayashi and K. Domen, An oxynitride, TaON, as an efficient water oxidation photocatalyst under visible light irradiation ($\lambda \leq$ 500 nm), *Chem. Commun.*, 2002, **2**(16), 1698–1699, DOI: 10.1039/B202393H.

30 G. Hitoki, A. Ishikawa, T. Takata, J. N. Kondo, M. Hara and K. Domen, Ta$_3$N$_5$ as a novel visible light-driven photocatalyst (λ < 600 nm), *Chem. Lett.*, 2002, **31**(7), 736–737, DOI: 10.1246/CL.2002.736.

31 K. Maeda, et al., Photocatalyst releasing hydrogen from water, *Nature*, 2006, **440**(7082), 295, DOI: 10.1038/440295A.

32 K. Maeda and K. Domen, Water oxidation using a particulate BaZrO$_3$-BaTaO$_2$N solid-solution photocatalyst that operates under a wide range of visible light, *Angew. Chem., Int. Ed.*, 2012, **51**(39), 9865–9869, DOI: 10.1002/ANIE.201204635.

33 X. Zong, et al., Photocatalytic water oxidation on F, N co-doped TiO$_2$ with dominant exposed {001} facets under visible light, *Chem. Commun.*, 2011, **47**(42), 11742–11744, DOI: 10.1039/C1CC14453G.

34 S. Ida, Y. Okamoto, M. Matsuka, H. Hagiwara and T. Ishihara, Preparation of tantalum-based oxynitride nanosheets by exfoliation of a layered oxynitride, CsCa 2Ta 3O$_{10-x}$N$_y$, and their photocatalytic activity, *J. Am. Chem. Soc.*, 2012, **134**(38), 15773–15782, DOI: 10.1021/JA3043678.

35 H. Kato, K. Asakura and A. Kudo, Highly efficient water splitting into H$_2$ and O$_2$ over lanthanum-doped NaTaO$_3$ photocatalysts with high crystallinity and surface nanostructure, *J. Am. Chem. Soc.*, 2003, **125**(10), 3082–3089, DOI: 10.1021/JA027751G.

36 S. Chen, et al., Nitrogen-doped layered oxide Sr$_5$Ta$_4$O$_{15-x}$N$_x$ for water reduction and oxidation under visible light irradiation, *J. Mater. Chem.*, 2013, **1**(18), 5651–5659, DOI: 10.1039/C3TA10446J.

37 K. Yoshioka, V. Petrykin, M. Kakihana, H. Kato and A. Kudo, The relationship between photocatalytic activity and crystal structure in strontium tantalates, *J. Catal.*, 2005, **232**(1), 102–107, DOI: 10.1016/J.JCAT.2005.02.021.

38 M. Kakihana and K. Domen, The synthesis of photocatalysts using the polymerizable-complex method, *MRS Bull.*, 2000, **25**(9), 27–31, DOI: 10.1557/MRS2000.176.

39 J. Shannon and L. Katz, A refinement of the structure of barium tantalum oxide, $Ba_5Ta_4O_{15}$, *Acta Crystallogr., Sect. B*, 1970, **26**(2), 102–105, DOI: 10.1107/S0567740870002017.

40 J. Huang, et al., Cs-Promoted ruthenium catalyst supported on $Ba_5Ta_4O_{15}$ with abundant oxygen vacancies for ammonia synthesis, *Appl. Catal., A*, 2021, **615**, 118058, DOI: 10.1016/J.APCATA.2021.118058.

41 P. Giannozzi, et al., QUANTUM ESPRESSO: a modular and open-source software project for quantumsimulations of materials, *J. Phys.: Condens. Matter*, 2009, **21**(39), 395502, DOI: 10.1088/0953-8984/21/39/395502.

42 J. P. Perdew, K. Burke and M. Ernzerhof, Generalized gradient approximation made simple, *Phys. Rev. Lett.*, 1996, 77(18), 3865, DOI: 10.1103/PhysRevLett.77.3865.

43 P. E. Blöchl, Projector augmented-wave method, *Phys. Rev. B: Condens. Matter Mater. Phys.*, 1994, **50**(24), 17953, DOI: 10.1103/PhysRevB.50.17953.

44 H. J. Monkhorst and J. D. Pack, Special points for Brillouin-zone integrations, *Phys. Rev. B: Condens. Matter Mater. Phys.*, 1976, **13**(12), 5188, DOI: 10.1103/PhysRevB.13.5188.

45 M. A. Green, Intrinsic concentration, effective densities of states, and effective mass in silicon, *J. Appl. Phys.*, 1990, **67**(6), 2944–2954, DOI: 10.1063/1.345414.

46 M. Mousavi, A. Habibi-Yangjeh and M. Abitorabi, Fabrication of novel magnetically separable nanocomposites using graphitic carbon nitride, silver phosphate and silver chloride and their applications in photocatalytic removal of different pollutants using visible-light irradiation, *J. Colloid Interface Sci.*, 2016, **480**, 218–231, DOI: 10.1016/J.JCIS.2016.07.021.

47 X. Huang, et al., Study on photocatalytic degradation of phenol by $BiOI/Bi_2WO_6$ layered heterojunction synthesized by hydrothermal method, *J. Mol. Liq.*, 2021, **322**, 114965, DOI: 10.1016/J.MOLLIQ.2020.114965.

48 R. S. Vařeková, Z. Jiroušková, J. Vaněk, Š. Suchomel and J. Koča, Electronegativity equalization method: parameterization and validation for large sets of organic, organohalogene and organometal molecule, *Int. J. Mol. Sci.*, 2007, **8**(7), 572–582, DOI: 10.3390/I8070572.

49 A. Sibari, Z. Kerrami, A. Kara and M. Benaissa, Strain-engineered p-type to n-type transition in mono-, bi-, and tri-layer black phosphorene, *J. Appl. Phys.*, 2020, **127**(22), 225703, DOI: 10.1063/1.5140360/1080490.

50 D. Chen and A. K. Ray, Removal of toxic metal ions from wastewater by semiconductor photocatalysis, *Chem. Eng. Sci.*, 2001, **56**(4), 1561–1570, DOI: 10.1016/S0009-2509(00)00383-3.

51 A. Hameed, M. A. Gondal, Z. H. Yamani and A. H. Yahya, Significance of pH measurements in photocatalytic splitting of water using 355 nm UV laser, *J. Mol. Catal.*, 2005, **227**(1–2), 241–246, DOI: 10.1016/J.MOLCATA.2004.10.053.

52 V. I. Anisimov, J. Zaanen and O. K. Andersen, Band theory and mott insulators: hubbard *U* instead of stoner *I*, *Phys. Rev. B: Condens. Matter Mater. Phys.*, 1991, **44**(3), 943, DOI: 10.1103/PhysRevB.44.943.

53 Z. Ech-charqy, A. El Badraoui, A. Elkhou, M. Ziati and H. Ez-Zahraouy, Effect of sulfur doping on the electronic structures, optical and photocatalytic properties of $KTaO_3$ perovskites: DFT calculations, *Chem. Phys.*, 2025, **596**, 112759, DOI: 10.1016/J.CHEMPHYS.2025.112759.

54 Y. Yuan, X. Han, H. Dong and X. Zhou, First-principles calculation of chalcogen-doped $Sr_2M_2O_7$ (M=Nb and Ta) for visible light photocatalysis, *J. Solid State Chem.*, 2022, **308**, 122905, DOI: 10.1016/J.JSSC.2022.122905.

55 M. H. Jameel, et al., A comparative DFT study of bandgap engineering and tuning of structural, electronic, and optical properties of 2D WS2, PtS2, and MoS_2 between WSe_2, $PtSe_2$, and $MoSe_2$ materials for photocatalytic and solar cell applications, *J. Inorg. Organomet. Polym. Mater.*, 2024, **34**(1), 322–335, DOI: 10.1007/S10904-023-02828-0/METRICS.

56 E. Sanville, S. D. Kenny, R. Smith and G. Henkelman, Improved grid-based algorithm for Bader charge allocation, *J. Comput. Chem.*, 2007, **28**(5), 899–908, DOI: 10.1002/JCC.20575.

57 L. Meng, et al., Piezo-photocatalytic synergetic for H_2O_2 generation *via* dual-pathway over Z-scheme ZIF-L/g-C_3N_4 heterojunction, *Nano Energy*, 2024, **128**, 109795, DOI: 10.1016/J.NANOEN.2024.109795.

58 A. Moreira Jorge Junior, K. Suarez Alcantara, Y. Chen, X. Fu and Z. Peng, A review on oxygen-deficient titanium oxide for photocatalytic hydrogen production, *Metals*, 2023, **13**(7), 1163, DOI: 10.3390/MET13071163.

59 A. Kumar and V. Krishnan, Vacancy engineering in semiconductor photocatalysts: implications in hydrogen evolution and nitrogen fixation applications, *Adv. Funct. Mater.*, 2021, **31**(28), 2009807, DOI: 10.1002/ADFM.202009807.

60 S. Parhoodeh and M. Kowsari, Synthesis, characterization and study of band gap variations of vanadium doped indium oxide nanoparticles, *Phys. B Condens. Matter*, 2016, **498**, 27–32, DOI: 10.1016/J.PHYSB.2016.06.020.

61 A. M. Schimpf, K. E. Knowles, G. M. Carroll and D. R. Gamelin, Electronic doping and redox-potential tuning in colloidal semiconductor nanocrystals, *Acc. Chem. Res.*, 2015, **48**(7), 1929–1937.

62 N. Baaalla, Y. Ammari, E. K. Hlil, R. Masrour, A. El Kenz and A. Benyoussef, Study of optical, electrical and photovoltaic properties of $CH_3NH_3PbI_3$ perovskite: *ab initio* calculations, *Phys. Scr.*, 2020, **95**(9), 095104, DOI: 10.1088/1402-4896/ABAE1E.

63 M. A. Rodriguez, T. J. Boyle, B. A. Hernandez, D. R. Tallant and K. Vanheusden, A new metastable thin-film strontium tantalate perovskite, *J. Am. Ceram. Soc.*, 1999, **82**(8), 2101–2105, DOI: 10.1111/J.1151-2916.1999.TB02047.X.

64 T. Takata, et al., Photocatalytic water splitting with a quantum efficiency of almost unity, *Nature*, 2020, **581**(7809), 411–414, DOI: 10.1038/S41586-020-2278-9.

65 Z. Chen, et al., Sr- and Co-doped $LaGaO_{3-\delta}$ with high O_2 and H_2 yields in solar thermochemical water splitting, *J. Mater. Chem. A*, 2019, **7**(11), 6099–6112, DOI: **10.1039/C8TA11957K**.

66 Y. Huang, et al., Insights into the role of S-Ti-O bond in titanium-based catalyst for photocatalytic CH_4 reforming: experimental and DFT exploration, *Chem. Eng. Sci.*, 2024, **289**, 119879, DOI: **10.1016/J.CES.2024.119879**.

67 M. El Akkel and H. Ez-Zahraouy, Tuning the photocatalytic performance of halide perovskites for efficient solar hydrogen production: a DFT study of $CsGeCl_{3-x}Xx$ (X = Br, I), *Solid State Commun.*, 2024, **394**, 115721, DOI: **10.1016/J.SSC.2024.115721**.

68 K. Ribag, et al., Computational investigation unveiling strain-engineered enhancements in the 2D InP photocatalyst for hydrogen production efficiency, *Comput. Condens. Matter*, 2025, **44**, e01096, DOI: **10.1016/J.COCOM.2025.E01096**.